

# **Ground Motion Amplification at Natural Rock Arches in the Colorado Plateau**

Riley Finnegan\*1<sup>©</sup>, Jeffrey R. Moore<sup>1</sup>, Paul R. Geimer<sup>1,2</sup>, Erin K. Bessette-Kirton<sup>1</sup>, and Alex Dzubay<sup>1</sup>

#### **Abstract**

Thousands of rock arches are situated within the central Colorado Plateau—a region experiencing small- to moderate-magnitude contemporary seismicity. Recent anthropogenic activity has substantially increased the seismicity rate in some areas, raising questions about the potential for vibration damage of natural arches, many of which have high cultural value. However, predictions of the vibration response and potential for damage at a given site are limited by a lack of data describing spectral amplification of ground motion on these landforms. We analyzed 13 sandstone arches in Utah, computing site-toreference spectral amplitude ratios from continuous ambient seismic data, and compared these to spectral ratios during earthquakes and teleseismic activity. We found peak ground velocities on arches at their dominant natural modes (in the range of 2-20 Hz) are ~20-180 times the velocity on adjacent bedrock, due to amplification arising from slender geometry and low modal damping (0.8%-2.7%). Ambient spectral ratios are generally 1.2-2.0 times the coseismic spectral ratios. Because arches experience highly amplified ground motion, the range of earthquakes considered potentially damaging may need to be revised to include lower-magnitude events. Our results have implications for conservation management of these and other culturally valuable landforms.

Cite this article as Finnegan, R., J. R. Moore, P. R. Geimer, E. K. Bessette-Kirton, and A. Dzubay (2022). Ground Motion Amplification at Natural Rock Arches in the Colorado Plateau, *The Seismic Record*. 2(3), 156–166, doi: 10.1785/0320220017.

**Supplemental Material** 

## Introduction

Seismic activity is a prominent contributor to the generation and propagation of damage in rock masses, aiding in the erosion and collapse of freestanding landforms (e.g., López et al., 2020; McPhillips and Scharer, 2021). Such features are likely to experience significant amplification of ground motion during earthquakes or other excitation of their normal modes (i.e., resonance), which can have important implications for coseismic rock fracturing. Relevant past studies have assessed amplification phenomena resulting from topography, near-surface soil, and weathered rock layers, as well as rock slope fracture networks in generating sometimes strongly amplified ground motions (siteto-reference spectral amplitude ratios of 10 or more) under ambient excitation and during earthquakes (e.g., Borcherdt, 1970; Boore, 1972; Çelebi, 1987; Havenith et al., 2002; Burjánek et al., 2010; Häusler et al., 2022; Weber et al., 2022). We hypothesize that rock arches are likely to amplify ground motion to an even greater degree than fractured rock slopes, in part, due

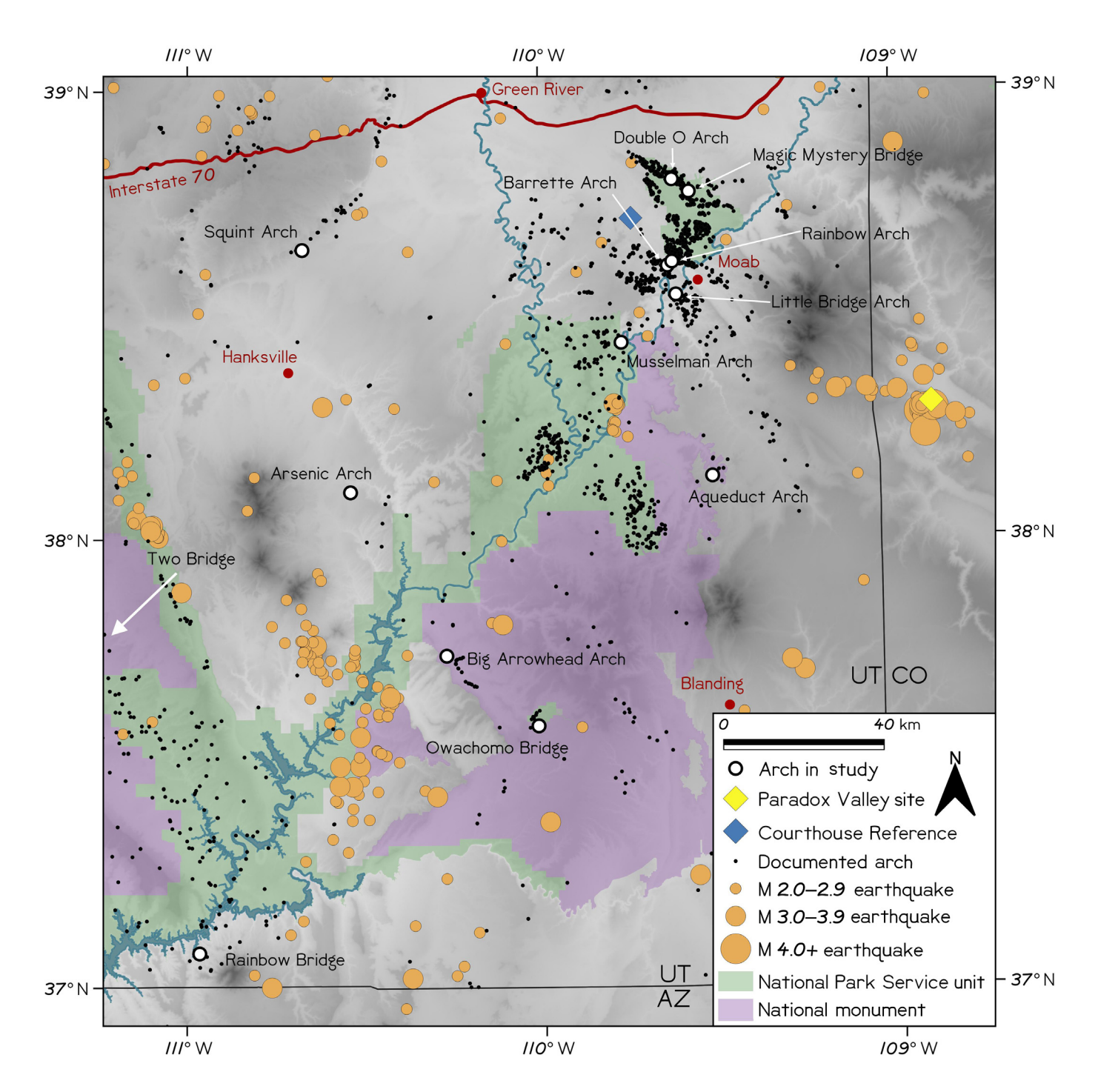
to their slenderness and low damping ratios (Moore *et al.*, 2019; Geimer *et al.*, 2020). However, aside from a single past measurement (Moore *et al.*, 2016), no studies have systematically assessed the seismic response of arches, in particular, quantifying spectral amplification of ground motion linked to resonance.

Large earthquakes have historically been rare in southeastern Utah, United States; consequently, arches in the region have likely evolved in a relatively seismogenically quiet setting (Wong and Humphrey, 1989; Fig. 1). However, growing

<sup>1.</sup> Department of Geology and Geophysics, University of Utah, Salt Lake City, Utah, U.S.A., https://orcid.org/0000-0003-3234-6439 (RF); https://orcid.org/0000-0001-5831-2048 (JRM); https://orcid.org/0000-0003-2627-5507 (PRG); https://orcid.org/0000-0002-2797-0694 (EKB-K); https://orcid.org/0000-0001-6656-312X (AD); 2. Los Alamos National Laboratory, Los Alamos, New Mexico, U.S.A.

<sup>\*</sup>Corresponding author: riley.finnegan@utah.edu

<sup>© 2022.</sup> The Authors. This is an open access article distributed under the terms of the CC-BY license, which permits unrestricted use, distribution, and reproduction in any medium, provided the original work is properly cited.



anthropogenic energy inputs, such as blasting and injection-induced earthquakes, are altering the vibration environment. For example, in 1991, the Bureau of Reclamation began injecting brine into a desalination well in Paradox Valley, Colorado, and has since recorded more than 6400 local earthquakes (Block *et al.*, 2017; Foulger *et al.*, 2018). In March 2019, the Paradox injection facility induced an  $M_{\rm w}$  4.5 earthquake (U.S. Geological Survey [USGS], 2022), with peak ground velocity (PGV) in the

**Figure 1.** Arches and earthquakes in southeastern Utah. Arch locations sourced from the World Arch Database (Van Bebber, 2013) (black dots), earthquakes (circles scaled by magnitude) are from the USGS (2022) Earthquake Catalog between December 1978 and February 2022.

Moab, Utah area ("Courthouse Reference": Fig. 1) exceeding 2 mm/s at frequencies coinciding with the natural modes of most arches, which may represent some of the strongest seismic shaking experienced by nearby landforms in decades. Although most of these induced earthquakes are not large enough to cause slope failure (e.g., Keefer, 1984), the increased rate of occurrence of these events, in addition to other sources, may contribute to an increased rate of progressive crack growth in arches and other rock landforms. Geotechnical analysis at a given site, however, is limited by an incomplete knowledge of the PGV experienced—a value needed to evaluate crack propagation using fracture mechanics models (Eppes and Keanini, 2017).

In this study, we measured site-to-reference spectral amplitude ratios for 13 natural arches in Utah, which have a broad range of spans and generally slender geometry. We calculated spectral ratios from ambient vibration data curated to minimize nearby human disturbances and wind excitation. We quantified the seismic response of the landforms, that is, PGV and amplification, through comparison of these ratios during ambient and coseismic periods. Our results help inform analyses of vibration damage to these and similar features, given an expected or experienced earthquake, blast, or other ground-borne vibration input, in support of conservation management of culturally valued landforms.

# **Study Sites**

We selected 13 natural arches, all formed in sandstones, to calculate ambient spectral amplitude ratios (Table 1 and Fig. 1; Fig. S1, available in the supplemental material to this article). The arches are in southern Utah on the traditional lands of the Hopi, Navajo, Pueblo, Southern Paiute, Ute, and Zuni peoples, and Rainbow Bridge and other arches are held in special regard by these groups (Stoffle et al., 2016). Many of these arches are popular tourist attractions, with some seeing millions of visitors each year (National Park Service, 2021). We selected these landforms to include a range of sizes, with spans between 3 and 83 m, as well as different geometries, from slender beam-like arches to more curved arches formed in alcoves. Through modal analysis (e.g., Geimer et al., 2020), we determined that the arches have fundamental or mode 2 natural frequencies between ~2 and 20 Hz (Table 1), with deflection polarity (i.e., vertical or horizontal) of the modes determined from polarization analysis.

#### Methods

We collected continuous ambient vibration measurements at arches and adjacent bedrock reference sites, the majority of which were overnight recordings (Table 1). We additionally feature a dataset with nearly continuous measurements spanning 15 months at Aqueduct Arch (data in winter months were sparse due to loss of solar power). We used three-component instruments (Nanometrics Trillium Compact 20 s seismometers or Fairfield Zland 5 Hz nodal geophones) to record ambient vibrations of the landforms and reference sites, with sampling rates between 100 and 250 Hz. We placed one instrument directly on each arch, leveled and aligned to magnetic north, and another on nearby bedrock (5-100 m away) that served as the reference, using the same sensor type paired for each measurement. We attempted to place the arch seismometer in the location experiencing the maximum fundamental mode deflection (e.g., top center of arch), but, due to limited access, a few datasets suffer from suboptimal sensor placement and thus do not record peak vibration amplitudes (Fig. S2). Some of the recordings captured earthquake activity, including local and regional earthquakes as well as teleseisms.

For ambient overnight measurements (≥12 hr long), we rotated velocity data to the arch's orientation from magnetic north and used either the transverse or vertical component for subsequent processing (Table 1), corresponding to the deflection polarity of the arch's dominant mode (i.e., natural frequency with the greatest spectral amplitude). We detrended and demeaned the data, removed the instrument response, and bandpass filtered to include the range of natural frequencies identified from spectral analysis (Fig. 2b; Fig. S3), and confirmed these using frequency-dependent polarization analysis and numerical modal analysis following Geimer et al. (2020) for the arches not previously studied. We calculated the velocity spectrogram using 10-s windows with 80% overlap, zeropadded by a factor of 2, and tapered with a Hanning taper. We divided the spectrogram into five-minute time blocks with no overlap. Dissimilar distance to an energy source, like a person walking near an arch, causes unequal excitation at the site and reference stations and invalidates the spectral ratios. Similarly, wind nonuniformly excites bedrock and arch geometries. To remove noisy periods in which wind or human activity adversely affected the data, we employed a reference site power threshold: if the average 5-15 Hz reference power exceeded the threshold over the five-minute time block, the block was excluded from further processing (Fig. S3). We determined the threshold empirically by selecting a decibel power value of -185 dB and then adjusted the value slightly to accommodate for differences in site noise conditions. The resulting range was between -175 and -189 dB, except for

List of Study Sites and Characteristics, Including Location, Natural Frequency of Interest (Fundamental Unless Marked by an Asterisk), Arch Span, Geologic Unit, and Duration of Each Measurement Table 1

Site Name	Location Latitude, Longitude (Decimal Degrees)	Component and Orientation if Applicable (° from MN)	Natural Frequency (Hz)	Span (m)	Geologic Unit	Record Duration (hh:mm)	Median Ambient Amplitude Ratio (Q1, Q3)	Earthquake Amplitude Ratio (Q1, Q3)	Damping (%)
Aqueduct Arch	38.1372, -109.5165	Transverse, 65°	~5	24	Wingate Sandstone	15 months*	30 <sup>†</sup> (25, 36)	18 <sup>†</sup> (15, 21)	0.9⁺
Arsenic Arch	38.1056, -110.5391	Transverse, 126°	6.2	ю	Navajo Sandstone	24:02 <sup>‡</sup>	97 (78, 140)		8.0
Barrette Arch <sup>§</sup>	38.6069, -109.6358	Vertical	5.0	38	Wingate Sandstone	18:55‡	32 (27, 38)		6:0
Big Arrowhead Arch	37.7396, –110.2708	Vertical	12.9	7	Cedar Mesa Sandstone	19:50	57 (47, 69)		<del>-</del> -
			9.6			24:00‡	70 (60, 80)		1.0
						24:00*	55 (48, 63)		1.0
Double O Arch <sup>§</sup>	38.7990, -109.6210	Transverse, 129°	2.0∥	20	Entrada Sandstone	40:50	62 (57, 69)	33	1.5
Little Bridge Arch	38.5423, -109.6128	Vertical	12.1	12	Cutler Formation	22:40	92 (73, 109)		2.0
Magic Mystery Bridge <sup>§</sup>	38.7714, -109.5730	Transverse, 112°	6.4	18	Curtis Formation	18:10 <sup>‡</sup>	62 (52, 70)		4.1
Musselman Arch	38.4359, -109.7698	Vertical	4.4∥	37	White Rim Sandstone	74:40	175 (150, 206)	89, 134	8.

Median ambient amplitudes and amplitudes during earthquakes when available are reported with damping. Multiple natural frequencies, durations, amplitude ratios, and damping ratios reported with damping. Multiple natural frequencies, durations, and lillium Compact seismometers. MN, magnetic north, Q1, first quartile, Q3, third quartile.

<sup>\*</sup>Suboptimal instrument placement on the landform for the measurement.

<sup>\*</sup>Measurement made with Fairfield Zland nodal geophones. †Median value across long-term measurement.

<sup>&</sup>lt;sup>§</sup>Not previously characterized by Geimer et al. (2020).

<sup>(</sup>Continued next page.)

List of Study Sites and Characteristics, Including Location, Natural Frequency of Interest (Fundamental Unless Marked by an Asterisk), Arch Span, Geologic Unit, and Duration of Each Measurement Table 1 (continued)

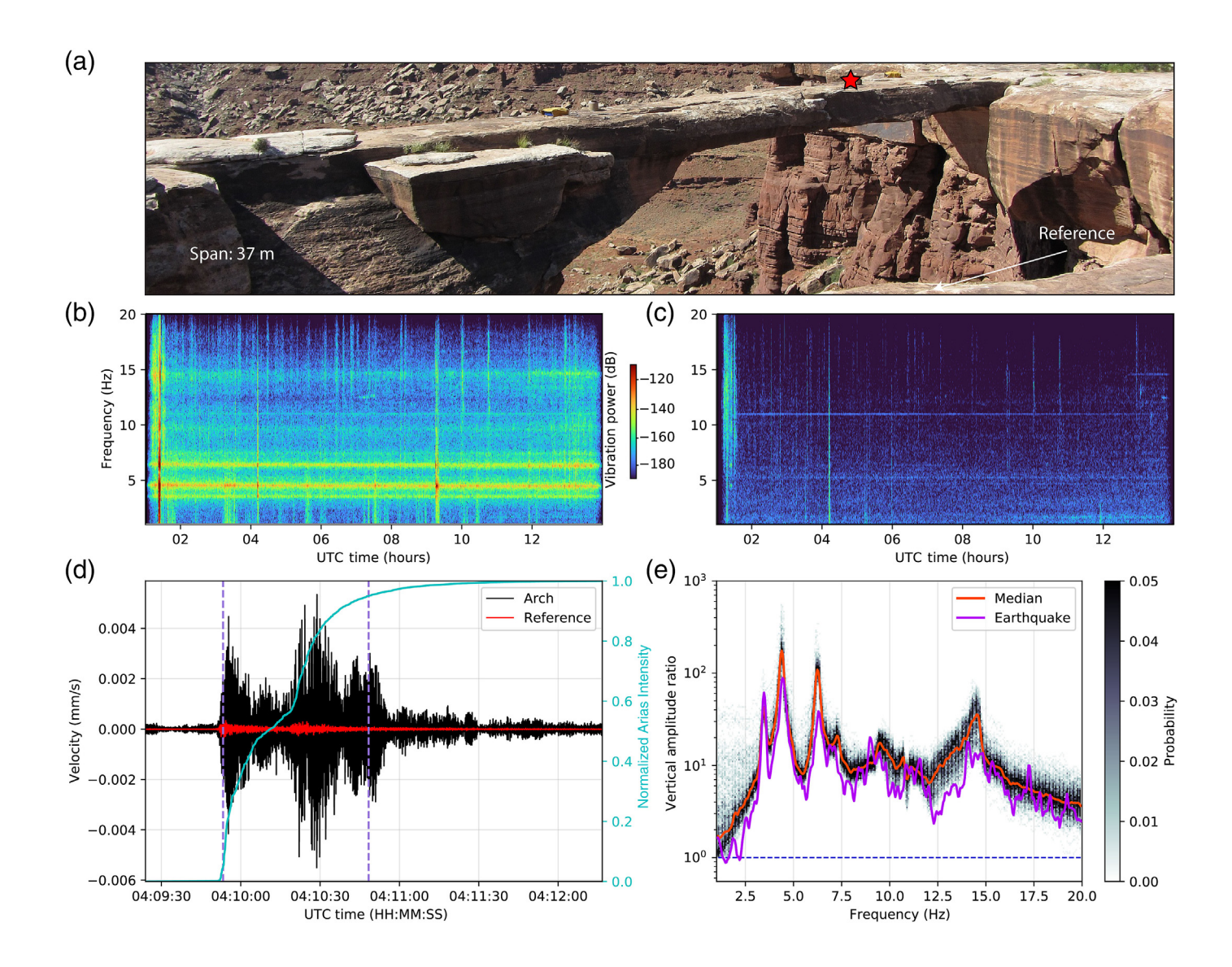
Site Name	Location Latitude, Longitude (Decimal Degrees)	Component and Orientation if Applicable (° from MN)	Natural Frequency (Hz)	Span (m)	Geologic Unit	Record Duration (hh:mm)	Median Ambient Amplitude Ratio (Q1, Q3)	Earthquake Amplitude Ratio (Q1, Q3)	Damping (%)
Owachomo Bridge	37.5823, -110.0141	Vertical	5.4	55	Cedar Mesa Sandstone	02:00	76 (60, 98)		6.1
			5.6			14:00	97 (87, 113)		2.7
Rainbow Arch	38.6156,109.6226	Vertical	20.6	4	Entrada Sandstone	00:35	91 (82, 110)		1.2
Rainbow Bridge	37.0774, –110.9643	Transverse, 54°	2.2	83	Navajo Sandstone	16:00*	46 (43, 51)	39, 81	1.0
Squint Arch	38.6465, -110.6739	Vertical	12.2	12	Navajo Sandstone	17:40	144 (126, 155)		<del></del>
			13.1			12:00	109 (66, 154)		6.0
Two Bridge	37.6212, –112.1639	Vertical	13.0	6	Claron Formation	14:30	53 (46, 59)	26	6:0
			13.6			19:15	43 (34, 53)		6.0
			13.7			19:40	17 (15, 20)		6.0

Median ambient amplitudes and amplitudes during earthquakes when available are reported with damping. Multiple natural frequencies, durations, amplitude ratios, and damping ratios reported for sites with repeat measurements. Differences in natural frequency between measurements at a single site arise due to seasonal temperature variations. Unless marked, measurements were made using Nanometrics Trillium Compact seismometers. MN, magnetic north; Q1, first quartile; Q3, third quartile.

<sup>\*</sup>Suboptimal instrument placement on the landform for the measurement.

<sup>†</sup>Median value across long-term measurement.

<sup>\*</sup>Measurement made with Fairfield Zland nodal geophones.  ${}^{\S} \text{Not}$  previously characterized by Geimer et al. (2020). IMode 2.



two noisy sites that required higher thresholds (Barrette Arch: -155 dB and Rainbow Arch: -141 dB),

For the retained time blocks, we converted decibel powers to amplitudes in each 10-s window and averaged the results to obtain amplitude spectra. We performed these steps for both arch and reference data, and then divided arch spectra by reference spectra to calculate spectral ratios. Next, we generated 2D histograms to quantify the results as probability density functions (Fig. 2e). We calculated the median ratio at the dominant natural frequency, and used the first and third quartiles to determine uncertainty. During each of the retained five-minute blocks, we calculated damping using the random decrement technique (Cole, 1973; Mikael *et al.*, 2013), in which an exponentially decaying sinusoid is fit to the impulse response derived from random noise, generated by stacking multiple bandpassed

Figure 2. Spectral amplification example. (a) Musselman Arch (Canyonlands National Park, Utah), red star is location of broadband seismometer, reference seismometer off-image. (b) Musselman Arch vertical velocity spectrogram from 21 June 2016 01:00 to 21 June 2016 14:00 (one night of the ~three-day measurement). (c) Bedrock reference spectrogram for the same time period as panel (b). Vibration power in panels (b) and (c) is given in decibel units relative to  $1 \text{ m}^2 \text{ s}^{-2} \text{ Hz}^{-1}$ . (d)  $M_1$  2.2 Panguitch, Utah earthquake, ~230 km from Musselman Arch, recorded on the arch and bedrock, filtered between 1 and 20 Hz. Normalized Arias Intensity is shown by the blue line, and the 5%-95% Arias duration of the earthquake is indicated by the dashed lines. (e) Probability density of arch-to-reference amplitude spectral ratios for the entire ~three-day recording, excluding windy or other noisy periods (see also Fig. S3). Spectral ratios peak at the natural frequencies previously identified for this arch by Geimer et al. (2020). Maximum median spectral ratio (175 at 4.4 Hz) and corresponding value during the  $M_{\rm L}$  2.2 earthquake (89 at 4.4 Hz) are included, along with a dashed line showing an ambient ratio of one. For additional details, see Figure S3.

time windows with identical starting conditions, relative to positive velocity crossing (Fig. S3). We used 15-cycle windows stacked over the five minutes, filtered around the dominant natural frequency, and reported the median damping ratio,  $\zeta$ —related to the quality factor,  $Q = \frac{1}{2\zeta}$ —for each arch.

For shorter measurements (≤2 hr long), we followed the same processing steps but divided the spectrogram into one-minute time blocks, instead of five minutes, to increase the number of ratios included in the histogram. For the 15-month Aqueduct Arch dataset, we designated 01:00–14:00 UTC (18:00–07:00 MST) as overnight for each day in the record and implemented the same processing as the overnight recordings, though we used 50% overlap instead of 80% to improve computation time. We excluded any nights with fewer than 12 retained five-minute time blocks from further processing, reducing 15 months of data to 389 nights.

When an earthquake was present and recorded clearly on the arch with detectable *P*- and *S*-wave arrivals, and contained spectral energy in the range of the arch's natural frequencies (Fig. S3g), we calculated arch-to-reference spectral ratios during the period of seismic activity. We used a short-time average/long-time average trigger to determine the arrival time at the nearby bedrock reference site. We coarsely estimated the duration of earthquake ground motion following Esteva and Rosenblueth (1964),

$$T_d = 0.02e^{0.74M} + 0.3\Delta, (1)$$

in which  $T_d$  is duration in seconds, M is earthquake magnitude, and  $\Delta$  is epicentral distance in kilometers, to trim our data. We then calculated the time-dependent Arias Intensity (Arias, 1970),  $I_A$ :

$$I_A(t) = \frac{\pi}{2g} \int_0^{T_d} a(t)^2 dt,$$
 (2)

to narrow in on a more precise value of earthquake duration over which we calculated the spectral ratio (*g* is gravitational acceleration, and *a* is ground acceleration). We normalized the Arias Intensity over time, and designated the start and end times of the earthquake at the arch from the 5%–95% bounds of total seismic energy accumulation (Trifunac and Brady, 1975; Fig. 2d). We then computed the spectral amplitude ratio over this time, treating the duration of the earthquake as a single window and following the same methods for the ambient overnight ratios.

For the 15-month dataset at Aqueduct Arch, we used libcomcat (USGS, 2020) to access the Advanced National

Seismic System Comprehensive Earthquake Catalog and search for earthquakes measured at the arch. We selected events using criteria designed to capture earthquakes recorded clearly at the arch and to increase the likelihood that the earthquake frequency content aligned with arch natural frequencies. We chose all earthquakes  $M \ge 4$  within a radius of 800 km from the arch,  $M \ge 3$  within 600 km,  $M \ge 2$  within 400 km, and  $M \ge 1$  within 100 km. This initial catalog included 379 earthquakes, which we reduced to 223 events based on clear P- and S-wave arrivals and data availability.

## **Results**

We computed ambient vibration spectral amplitude ratios from 19 datasets at 13 sandstone arches in Utah, with resulting median amplification factors at the dominant modes ranging between ~20 and 180 (Table 1). Modal damping ratios for the arches are low, between 0.8% and 2.7% (Q equivalent of 18.5–62.5) (Table 1), and we found no clear correlation between amplification and damping (compare to Moore et al., 2019). Our probabilistic spectral ratios demonstrate that amplification factors are the maximum at the dominant natural modes of the arch, that is, resonance is excited at specific natural frequencies. These range between ~2 and 20 Hz, the majority of which are fundamental modes. In addition, the majority of the analyzed natural modes are vertically polarized, though a few are horizontal, such as the ~5-Hz fundamental mode at Aqueduct Arch. We resolved higher-order modes at all sites, though our analysis only focuses on the dominant natural frequency that produces the largest amplification at each arch.

We recorded six earthquakes during our overnight measurements on arches, which resulted in spectral amplification factors between 18 and 134 (Table 1). Notably, at Musselman Arch, we recorded one local earthquake and one teleseism. The  $M_{\rm L}$  2.2 earthquake, located in Utah ~230 km from Musselman Arch, produced a peak spectral ratio of 89 (see Fig. 2), whereas the  $M_{\rm w}$  3.4 teleseism, originating in Oklahoma near an injection site 1010 km from the arch, produced a peak ratio of 134. Ambient site-to-reference spectral ratios were 1.2-2.0 times the ratios during earthquakes at each site, aside from one earthquake at Rainbow Bridge and one at Two Bridge, which were 1.8 and 1.5 times the ambient ratios, respectively (Table 1). We recorded over two hundred earthquakes (M 1.2-5.0) during our long-term deployment at Aqueduct Arch, in which the sensor was not ideally situated to measure the maximum modal deflection. There, compiled arch-to-bedrock amplifications had a median value of 18 during seismic activity,

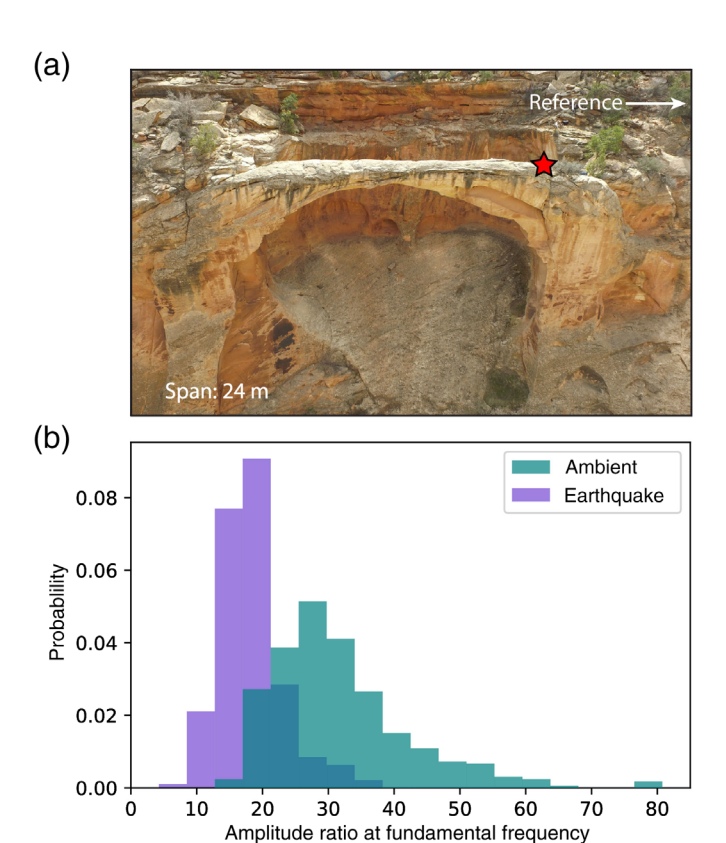


**Figure 3.** Aqueduct Arch spectral amplitude ratios for the dominant (and fundamental) mode of  $\sim$ 5 Hz (precise frequency varies seasonally). (a) Seismometer location on Aqueduct Arch (red star) was poorly situated to record peak vibration amplitude of the fundamental mode (see Fig. S2). Reference sensor is  $\sim$ 100 m to the west (indicated by arrow). (b) Histogram of amplitude ratios over the 15-month measurement campaign. Ambient amplitude ratios are taken from overnight measurements (n = 389, median = 30), whereas earthquake amplitude ratios are from the identified events (n = 223, median = 18).

compared to a median ambient value of 30 (Table 1 and Fig. 3). Spectral ratios for 195 of the 223 recorded earthquakes were lower than those measured during ambient nighttime conditions on the same day.

## Discussion

Median arch-to-bedrock spectral amplitude ratios for the 13 study sites ranged between ~20 and 180 (Fig. 4). However, measuring the maximum spectral amplification of an arch requires precise placement of the seismometer at the location of the greatest modal deflection, thus some of our reported values are lower bounds. For example, a simultaneous measurement at Big Arrowhead Arch with one sensor positioned at the point of the maximum deflection for the fundamental mode

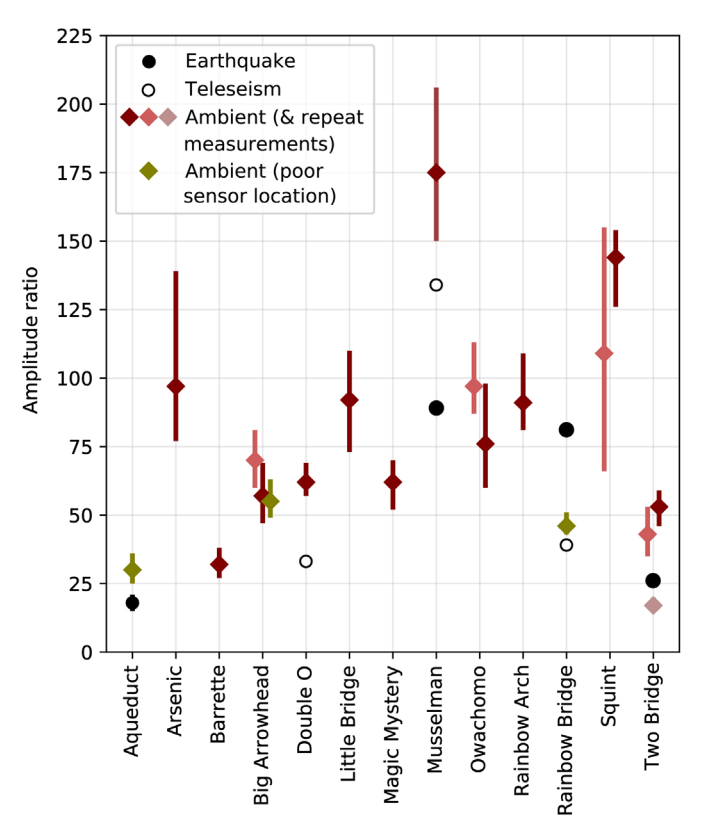


**Figure 4.** Summary of arch-to-reference amplitude spectral ratios at the dominant natural frequency for each site (see Table 1). Ambient median values are presented with bars extending between the first and third quartiles. Spectral ratios calculated during earthquakes are included when present, with median and quartile bars for the long-term Aqueduct Arch measurement that includes hundreds of earthquakes. Poor sensor location indicates sensor placements not measuring the landform's maximum modal displacement; these ratios are thus lower bound values.

(arch center) and another closer to the arch abutment yielded a center amplitude ratio ~27% greater than the uncentered value. This indicates the spectral ratios reported for Aqueduct Arch and Rainbow Bridge, where sensor placement was suboptimal (see Fig. 3a), underrepresent maximum values. This is also supported by numerical predictions of modal deflection for Aqueduct Arch, where peak displacement at the fundamental mode is approximately five times the displacement at the location of the seismometer near the abutment (Fig. S2).

We anticipated that modal displacements would be greater for lower arch stiffness values, leading to higher amplification. To test this, we analyzed a subset of the studied arches with geometries similar to a rectangular beam fixed at both the ends, in which analytical theory predicts the bending, or deflection stiffness, is related to both Young's modulus and beam geometry (Gere and Timoshenko, 1997). We found that, in general, amplification for beam-like arches increased as the estimated bending stiffness decreased, as expected. However, large scatter resulted from site-specific geometrical and material property variations, the small sample size of the land-forms studied, as well as variability and uncertainty inherent in our spectral ratio measurements, causing overall poor correlation. We attribute the lack of an inverse relationship between damping and spectral amplification to these same factors.

We applied our methodology for computing ambient siteto-reference ratios to other rock landforms, producing similar results as the studied arches. For example, analysis of a ~36-mhigh rock tower yielded a median amplification ratio of 45, whereas a ~70-m-high toppling rock slab produced a median ratio of 78. A previous study of the 120-m-high Castleton Tower by Moore et al. (2019) predicted spectral amplification of ~70 at the fundamental frequency assuming a simple multiple-degree-of-freedom system, which is within the range measured for the arches; however, the value could not be calculated due to sustained winds during the measurement. Finzi et al. (2019) similarly reported an amplification factor of 100 for a rock pillar compared to a nearby cliff, though it is not clear if windy times were removed from this calculation. These examples support broad application of our methodology to other landforms, such as rock towers and hoodoos, as well as ancient cultural sites.

We captured six earthquakes during the overnight arch deployments and >200 earthquakes throughout the 15-month Aqueduct Arch measurement. Generally, ambient arch-toreference spectral ratios were 1.2-2.0 times the corresponding coseismic values, though the specific reasons for this difference remain unclear. Potentially: (1) the seismic records, being short in duration, had relatively few data points resulting in large scatter, inadvertently biasing our results. However, Figure 3b shows the coseismic spectral ratios are closely distributed about their median, indicating these were not adversely affected by shorter time blocks. (2) A predicted damping increase during periods of relatively large ground motion could result in decreased amplification (Satake et al., 2003). However, damping ratios at Aqueduct Arch were comparable in both ambient and coseismic conditions (Fig. S4). (3) The employed reference threshold was too lenient, allowing periods of slight wind gusts to be included in the ambient ratios raising these values. We tested progressively increasing the strictness of the reference power threshold at several sites and found that the median ambient ratio did not progressively decrease, although the

greater range of values for ambient data (Fig. 3b) may reflect a persistent influence of slight wind gusts producing higher amplification ratios. (4) Different types of seismic waves in an earthquake could excite an arch differently, that is, surface waves are more effective at exciting resonance than body waves. However, further subwindowing our earthquake records will produce a large amount of scatter, making this difference difficult to detect.

We had a bedrock reference seismometer ("Courthouse Reference" in Fig. 1) deployed (not on an arch) during the 4 March 2019 M<sub>w</sub> 4.5 Paradox Valley earthquake, where we measured PGV of 1 mm/s in the 1-20 Hz band at an epicentral distance of 85 km. Although this PGV is low for consideration of rock damage, our results indicate that amplification of ground motion by natural arches can magnify low PGV levels to a range that might cause damage to geologic landforms and ancient structures (estimated as >2 mm/s, see Whiffin and Leonard, 1971; Hanson et al., 1991; Hendricks, 2002; Moore, 2018). Specifically, the Paradox Valley earthquake at these epicentral distances (which incorporates most arches in Arches National Park) could have generated arch PGV >1 cm/s. These elevated shaking levels likely contribute to increased subcritical crack growth rates (Eppes and Keanini, 2017), which can impact the long-term structural health of an arch. The USGS ShakeMap (2017) for the  $M_{\rm w}$  4.5 earthquake predicted PGV near our instrument of 0.5-1.0 mm/s, in agreement with our measured value, indicating possible use of this tool combined with our spectral amplification dataset to estimate vibration velocities experienced by an arch during an earthquake. Amplification during strong ground motion could be different than measured in this study under relatively weak excitation; however, our results nonetheless suggest that the earthquake magnitude of concern for structural damage may be lower than previously considered, and that smaller earthquakes could impact the structural health of culturally valuable rock landforms.

### **Conclusions**

We measured ambient vibrations of 13 natural rock arches and nearby bedrock to compute arch-to-reference spectral amplitude ratios. We found that under ambient conditions in the absence of wind, arches vibrate at their dominant natural frequency at amplitudes  $\sim 20-180$  times that of adjacent bedrock. Spectral amplitude ratios during ambient conditions are generally 1.2–2.0 times the coseismic ratios, which helps inform future use of ambient spectral ratios to predict landform vibration

response to incoming energy from measurements at bedrock stations. Our methodology is applicable to other landforms, as well as historic cultural sites, and can be used beyond earth-quake risk assessments, for example, vibration risk management for blasting or road and construction work. The large spectral amplification of ground motion generated during resonance of arches suggests that although smaller-magnitude earthquakes may not result in complete failure, they could contribute to internal fracture growth that may hasten landform collapse. The amplitude ratios we presented provide a baseline for predicting arch response to seismic and other ground-borne energy sources in support of site-specific geotechnical analyses.

## **Data and Resources**

All data from Aqueduct Arch and the Courthouse Reference station are available from the International Federation of Digital Seismograph Networks: doi: 10.7914/SN/5P\_2013. All other data are available at doi: 10.7278/S50d-n0gv-h76g. The supplemental material includes figures providing details on field sites, modeled arch displacements, data processing, and damping.

# **Declaration of Competing Interests**

The authors acknowledge that there are no conflicts of interest recorded.

# Acknowledgments

The authors thank the Hopi, Navajo, Southern Paiute, Ute, and Zuni tribes, along with the National Park Service, for allowing access to Rainbow Bridge. The Charles Redd Center for Western Studies and the National Science Foundation (Grant Number EAR-1831283) supported this study. Ammon Hatch, Anna Stanczyk, Ashley Russon, Ben White, Brendon Quirk, Clayton Russell, Holly Hurtado, Naveed Aghdassi, and Weston Manygoats provided field assistance. Keith Koper, Kris Pankow, Clotaire Michel, and two anonymous reviewers gave valuable input for this article.

#### References

- Arias, A. (1970). A Measure of Earthquake Intensity in Seismic Design of Nuclear Power Plants, R. J. Hansen (Editor), The Massachusetts Institute of Technology Press, Cambridge, Massachusetts.
- Block, L., M. Meremonte, C. Wood, G. Besana-Ostman, and Bureau of Reclamation (2017). 2016 Annual report Paradox Valley Seismic Network, Paradox Valley Unit, Colorado, *Technical Memorandum* TM-85-833000-2017-22.
- Boore, D. M. (1972). A note on the effect of simple topography on seismic SH waves, *Bull. Seismol. Soc. Am.* **62**, 275–284.

- Borcherdt, R. D. (1970). Effects of local geology on ground motion near San Francisco Bay, *Bull. Seismol. Soc. Am.* **60**, no. 1, 29–61.
- Burjánek, J., G. Gassner-Stamm, V. Poggi, J. R. Moore, and D. Fäh (2010). Ambient vibration analysis of an unstable mountain slope, *Geophys. J. Int.* **180**, no. 2, 820–828.
- Çelebi, M. (1987). Topographic and geological amplification determined from strong-motion and aftershock records of the 3 March 1985 Chile earthquake, *Bull. Seismol. Soc. Am.* 77, 1147–1167.
- Cole, H. A. (1973). On-line failure detection and damping measurement of aerospace structures by random decrement signatures, *Contract Rept. NASA-CR-2205*.
- Eppes, M.-C., and R. Keanini (2017). Mechanical weathering and rock erosion by climate-dependent subcritical cracking, *Rev. Geophys.* **55**, 470–508, doi: 10.1002/2017RG000557.
- Esteva, L., and E. Rosenblueth (1964). Espectros de temblores a distancias moderadas y grandes, *Boletin Sociedad Mexicana de Ingenieria Sismica* 2, no. 1, 1–18 (in Spanish).
- Finzi, Y., N. Ganz, O. Dor, M. Davis, O. Volk, S. Langer, R. Arrowsmith, and M. Tsesarsky (2019). Stability analysis of fragile rock pillars and insights on fault activity in the Negev, Israel, J. Geophys. Res. 125, e2019JB019269, doi: 10.1029/2019JB019269.
- Foulger, G. R., M. P. Wilson, J. G. Gluyas, B. R. Julian, and R. J. Davies (2018). Global review of human-induced earthquakes, *Earth Sci. Rev.* 178, 438–514.
- Geimer, P. R., R. Finnegan, and J. R. Moore (2020). Sparse ambient resonance measurements reveal dynamic properties of freestanding rock arches, *Geophys. Res. Lett.* doi: 10.1029/2020GL087239.
- Gere, J. M., and S. P. Timoshenko (1997). *Mechanics of Materials*, PWS Pub. Co., Boston, Massachusetts.
- Hanson, C. E., K. W. King, M. E. Eagan, and R. D. Horonjeff (1991).
  Aircraft Noise Effects on Cultural Resources: Review of Technical Literature, HMMH Rept. No. 290940.04-1 for National Park Service, US Department of the Interior, Lexington, Massachusetts.
- Häusler, M., V. Gischig, R. Thöny, F. Glüer, and D. Fäh (2022). Monitoring the changing seismic site response of a fast-moving rockslide (Brienz/Brinzauls, Switzerland), *Geophys. J. Int.* 229, no. 1, 299–310, doi: 10.1093/gji/ggab473.
- Havenith, H. B., D. Jongmans, E Faccioli, K. Abdrakhmatov, and P. Y. Bard (2002). Site effect analysis around the seismically induced Ananevo rockslide, Kyrgyzstan, *Bull. Seismol. Soc. Am.* **92**, no. 8, 3190–3209.
- Hendricks, R. (2002). Transportation Related Earthborne Vibrations (Caltrans Experiences), Technical Advisory, Vibration TAV-02-01-R9601, 2002, California Department of Transportation, Division of Environmental Analysis, Sacramento, California.
- Keefer, D. K. (1984). Landslides caused by earthquakes, *Geol. Soc. Am. Bull.* **95**, no. 4, 406–421.
- López, A. M., K. S. Hughes, and E. Vanacore (2020). Puerto Rico's winter 2019–2020 seismic sequence leaves the island on edge, *Temblor* doi: 10.32858/temblor.064.
- McPhillips, D., and K. M. Scharer (2021). Survey of fragile geologic features and their quasi-static earthquake ground-motion constraints, southern Oregon, *Bull. Seismol. Soc. Am.* doi: 10.1785/0120200378.

- Mikael, A., P. Gueguen, P. Y. Bard, P. Roux, and M. Langlais (2013). The analysis of long-term frequency and damping wandering in buildings using the random decrement technique, *Bull. Seismol. Soc. Am.* **103**, no. 1, 236–246.
- Moore, J. R. (2018). Rainbow Bridge Vibration Risk Assessment: Ambient Vibration Testing and Computer Modeling Results for Rainbow Bridge, Natural Res. Rept. NPS/RABR/NRR-2018/1617, National Park Service, Fort Collins, Colorado, 70 pp.
- Moore, J. R., P. R. Geimer, R. Finnegan, and C. Michel (2019). Dynamic analysis of a large freestanding rock tower (Castleton Tower, Utah, USA), *Bull. Seismol. Soc. Am.* doi: 10.1785/0120190118.
- Moore, J. R., M. S. Thorne, K. D. Koper, J. R. Wood, K. Goddard, R. Burlacu, S. Doyle, E. Stanfield, and B. White (2016). Anthropogenic sources stimulate resonance of a natural rock bridge, *Geophys. Res. Lett.* 43, 9669–9676, doi: 10.1002/2016GL070088.
- National Park Service (2021). Arches National Park annual park recreation visits, NPS Stats, Stats-2.7.1.17543\_20191220: 12:49:45.
- Satake, N., K.-I. Suda, T. Arakawa, A. Sasaki, and Y. Tamura (2003). Damping evaluation using full-scale data of buildings in Japan, *J. Struct. Eng.* **129**, no. 4, doi: 10.1061/(ASCE)0733-9445(2003) 129:4(470).
- Stoffle, R., E. Pickering, K. Brooks, C. Sittler, and K. Van Vlack (2016). Ethnographic Overview and Assessment for Arches National Park, Bureau of Applied Research in Anthropology, University of Arizona, Tucson, Arizona.

- Trifunac, M. D., and A. G. Brady (1975). A study on the duration of strong earthquake ground motion, *Bull. Seismol. Soc. Am.* **65**, no. 3, 581–626, doi: 10.1785/BSSA0650030581.
- U.S. Geological Survey (USGS) (2017). ShakeMap—Earthquake ground motion and shaking intensity maps, U.S. Geol. Surv. doi: 10.5066/ F7W957B2.
- U.S. Geological Survey (USGS) (2020). libcomcat v2.0 [code], doi: 10.5066/P91WN1UQ.
- U.S. Geological Survey (USGS) (2022). Earthquake catalog, available at https://earthquake.usgs.gov/earthquakes/search/ (last accessed February 2022).
- Van Bebber, T. (2013). World arch database [Software]. v3.5.4.0, Stone Canyon Adventures, available at https://arches.stonecanyonadventures.com (last accessed January 2022).
- Weber, S., J. Beutel, M. Häusler, P. R. Geimer, D. Fäh, and J. R. Moore (2022). Spectral amplification of ground motion linked to resonance of large-scale mountain landforms, *Earth Planet. Sci. Lett.* **578**, doi: 10.1016/j.epsl.2021.117295.
- Whiffin, A. C., and D. R. Leonard (1971). A Survey of Traffic-Induced Vibrations, RRL Report LR418, Road Research Laboratory, Crowthorne, England, 57 pp.
- Wong, I. G., and J. R. Humphrey (1989). Contemporary seismicity, faulting, and the state of stress in the Colorado plateau, *Geol. Soc. Am. Bull.* **101**, no. 9, 1127–1146.

Manuscript received 20 April 2022 Published online 7 July 2022